Weierstraß-Institut
für Angewandte Analysis und Stochastik

im Forschungsverbund Berlin e.V.

Longitudinal modes of multisection semiconductor lasers and their dynamics

Mindaugas Radziunas[1], Hans-Jürgen Wünsche[2]

submitted: 26 May 2004

[1] Weierstraß-Institut
     für Angewandte Analysis und Stochastik
     Mohrenstrasse 39
     D – 10117 Berlin
     Germany
     E-Mail: radziuna@wias-berlin.de

[2] Humboldt-Universität zu Berlin
     Institut für Physik
     Invalidenstr. 110
     D – 10115 Berlin
     Germany
     E-Mail: wuensche@physik.hu-berlin.de

W I A S

Abstract

We simulate and analyse a 1D-PDE model describing the dynamics of multisection semiconductor lasers. We demonstrate how a semi-analytical computation of the spectrum and the corresponding eigenfunction expansion of the computed solutions provides a useful information allowing to achieve a better understanding of the laser dynamics. Basic algorithms implemented into a corresponding software tool are described.

1   Introduction

Multisection semiconductor lasers are useful for different purposes. Examples are wavelength tuning [1], chirp reduction [2], enhanced modulation bandwidths [3, 4], mode-locking of short pulses [5], and frequency-tunable self-pulsations [6, 7, 8, 9].

A deep understanding of these devices is required when designing them for specific functionalities. For these purposes we have developed a hierarchy of models and a corresponding software *LDSL-tool* (abbreviation for (L)ongitudinal (D)ynamics in multisection (S)emiconductor (L)asers). This software is based on the system of hyperbolic partial differential Travelling Wave equations [10] for the spatio-temporal distribution of the optical field in the laser, nonlinearly coupled to ordinary differential equations for carrier densities and material polarization in the active parts of the devices [11]. Direct numerical integration of the model equations and a comprehensive data post-processing make our software a powerful tool well suited for simulation and analysis of different dynamical effects experimentally observed in semiconductor lasers [7, 8, 9, 12, 13, 14, 15]. In this report we put special emphasis on the possibilities of *LDSL-tool* to analyse the dynamics in terms of longitudinal modes [8, 12, 13, 15, 16].

The concept of optical modes plays an outstanding role for understanding lasers in general. They represent the natural oscillations of the electromagnetic field and determine the optical frequency and the lifetime of the photons contained in the given laser cavity. In multisection lasers, the modes respond exceptionally sensitive to variations of the carrier distributions. Not only the overall number of photons is involved here in the dynamics, but also the internal spatial distribution of the photons. We will show, how computation and analysis of instantaneous modes and field decomposition into these changing modal components help to understand the complicated dynamics of multisection lasers. This analysis allows us to determine the dimensionality of the observed dynamics as well as to understand sometimes

1

quite curious temporal profiles and properties of the optical field power in these dynamical regimes.

Supplementing simulation calculations with a consequent mode analysis provide a deeper insight into the nature of different operating regimes and allow to understand the mechanisms of transitions between different regimes. This concept has been successfully used to design lasers with specific dynamics [12, 13], to analyse limitations of fabricated lasers operating at the required dynamical regime, and to improve the design of these lasers [8, 14, 15]. In this paper we shall illustrate the usefulness of mode analysis by a few examples. In particular, we shall consider two different self-pulsating regimes of the three-section structure sketched in Fig. 1a. Multisection lasers of this type can serve as optical clock in all-optical signal processing [6, 17].

The paper is organized as follows. The model and the basic ideas of mode analysis are introduced step by step and illustrated with example calculations in Sections 2 to 7. Details are suppressed here as much as possible in favour of clarity. Using all ideas introduced before, we analyse the dynamics of another laser example in the Sections 8 and 9. After summarising conclusions in Section 10 we finish with mathematical details and a description of the adopted numerical schemas in Appendix Section 11.

2   Travelling Wave Model

The calculation of spatio-temporal carrier and photon distributions in a semiconductor laser is in general a complicated multidimensional problem. Fortunately, the corresponding transverse distributions are mostly fixed by the device design and confined to regions small compared with the laser length. Under these circumstances, the transverse problem can be treated independently [18, 19] and will not be considered here. We regard laser devices of this type consisting of m successively located sections S_k with lengths L_k (see Fig. 1b). Here and in the sequel, the subscript indices $_k$ attribute quantities to the section S_k. The considered two
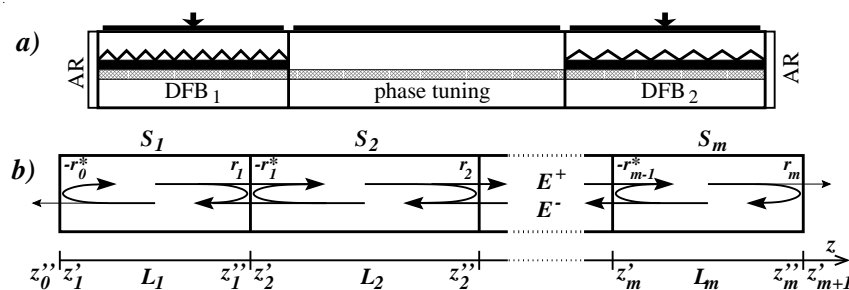

Figure 1: Schemes of multisection semiconductor lasers. Panel a: scheme of the 3 section laser treated as example in this paper. Panel b: general scheme of a multisection laser composed of m sections with a sketch of counterpropagating optical waves. Details are described in the text.

counterpropagating optical waves are represented by their slowly varying amplitudes

2

$E^+(z,t), E^-(z,t)$, a pair of complex valued functions of the longitudinal coordinate z and the time t. The optical field drives the complex material polarization functions $p^+(z,t), p^-(z,t)$ and interacts with the real carrier density function $n(z,t)$. These quantities obey the travelling wave (TW) model equations (see, e.g. [10, 11]), which can be written in the compact form

$$-i\frac{\partial}{\partial t}\Psi(z,t) = H(\beta,z)\Psi + F_{sp}, \tag{1}$$

$$\frac{\partial}{\partial t}n(z,t) = \mathcal{N}(n,|E|^2,\Re e(E^*p),z). \tag{2}$$

The wave function Ψ is the four-component column vector $\Psi = (E^+, E^-, p^+, p^-)^T$ of the optical and polarisation amplitudes, where E satisfies boundary conditions at the interfaces of the sections and facettes. The superscripts ^{T} and * denote the transpose and complex conjugation, respectively. Accordingly, the evolution operator $H(\beta,z)$ is a 4×4 matrix containing first order derivatives with respect to the space coordinate z within the sections. Details of this operator as well as of the boundary conditions are specified in the following Section 3. Here, we emphasize only that its dependence on the carrier densities and the optical fields is fully mediated by the distribution of the complex propagation parameter β defined in Equ. (3) along the optical waveguide. The inhomogeneity $F_{sp} = (F_{sp}^+, F_{sp}^-, 0, 0)^T$ represents the spontaneous emission noise added to the guided waves. It is a stochastic force in the sense of a Langevin calculus which has been described elsewhere (see, e.g., [14, 20] for more details). The right-hand side of the carrier rate equation (2) comprises pumping by injection, spontaneous and stimulated recombination and is also described in detail in Section 3.

More details of the model and of the used set of parameters will be specified in the next section. Readers more interested in examples and possible applications of our analysis can skip it and continue reading with Section 4.

3 Model details and parameters

3.1 Model details

The linear operator $H(\beta,z)$ in Equ. (1) is defined as follows. If z belongs to the interior of a device section, it holds

$$H(\beta,z) \stackrel{def}{=} \begin{pmatrix} H_0(\beta,z)+\frac{iv_{gr}\bar{g}}{2}\mathcal{I} & -\frac{iv_{gr}\bar{g}}{2}\mathcal{I} \\ -i\bar{\gamma}\,\mathcal{I} & (\bar{\omega}+i\bar{\gamma})\mathcal{I} \end{pmatrix},$$

$$H_0(\beta,z)E \stackrel{def}{=} v_{gr}\begin{pmatrix} i\partial_z-\beta & -\kappa^-(z) \\ -\kappa^+(z) & -i\partial_z-\beta \end{pmatrix}\begin{pmatrix} E^+ \\ E^- \end{pmatrix},$$

$$\beta(n,|E|^2) \stackrel{def}{=} \delta - \frac{i\alpha}{2} + \frac{ig'(n-n_{tr})}{2(1+\varepsilon_G|E|^2)} + \frac{\alpha_H g'(n-n_{tr})}{2(1+\varepsilon_I|E|^2)}. \tag{3}$$

3

Here, $\mathcal{I}$ is a 2×2 identity matrix, $\kappa^{\pm}$ are, in general, spatially dependent complex coupling factors between the counterpropagating fields in sections with Bragg grating, v_{gr} is group velocity. The parameters δ, α, g', n_{tr}, α_H, ε_G and ε_I represent static detuning, internal optical losses, effective differential gain[1] including the transverse confinement factor, transparency carrier density, Henry linewidth enhancement factor, gain and index compression factors, respectively. The effective inclusion of the polarization equations is used to model the frequency dependence of the optical gain close to its maximum. It corresponds to a Lorentzian gain peak with amplitude $\bar{g} > 0$ and full width at half maximum $2\bar{\gamma}$ in frequency domain, which is centered at the optical frequency $\bar{\omega}$ [11]. At the same time, the polarisation equations automatically cause a dispersion of the effective refractive index according to the Kramers-Kronig relation.

The boundary conditions for the function E at the interfaces and facettes are given by

$$
\begin{aligned}
E^+(z'_{k+1}, t) &= -r_k^* E^-(z'_{k+1}, t) + t_k E^+(z''_k, t) \\
E^-(z''_k, t) &= r_k E^+(z''_k, t) + t_k E^-(z'_{k+1}, t).
\end{aligned} \tag{4}
$$

Here z'_k and z''_k indicate the left and right edges of the section S_k. Accordingly, z''_k and z'_{k+1} denote the joining edges of two neighbouring sections S_k and S_{k+1} and correspond to the same spatial coordinate (see also the notations in Fig. 1b). The complex coefficients r_k, $-r_k^*$ and the real number $t_k = \sqrt{1 - |r_k|^2}$ denote forward to backward, backward to forward field reflectivities at the junction of sections S_k and S_{k+1}, and field transmission coefficients through this junction, respectively (see [20, 21] and Fig. 1b). The quantities $E^-(z''_0, t)$ and $E^+(z'_{m+1}, t)$ represent the amplitudes of the fields emitted at the facettes. Accordingly, $E^+(z''_0, t)$ and $E^-(z'_{m+1}, t)$ are the amplitudes of possible incoming fields at the same facettes. In this paper, we do not consider optical injections and set these values to zero.

By proper scaling of the wave function Ψ, $|E(z, t)|^2$ is the local photon density, i.e., the local power at z divided by $\hbar v_{gr} \sigma c_0 / \lambda_0$, where $\hbar$ is the Planck constant, c_0 is the speed of light in vacuum and λ_0 is the central wavelength. Now the function $\mathcal{N}$ at the right-hand side of carrier rate equation (2) can be defined as follows:

$$
\begin{aligned}
\mathcal{N}(n, |E|^2, \Re e(E^* p), z) &\overset{def}{=} \frac{I}{eL\sigma} + \frac{U'_F}{eL\sigma r_s}\left(\frac{1}{L}\int_S n\, dz - n\right) - \\
&- \left(An + Bn^2 + Cn^3\right) - v_{gr}\left[\left(\frac{g'(n - n_{tr})}{1 + \varepsilon_G|E|^2} - \bar{g}\right)|E|^2 + \bar{g}\Re e(E^* p)\right].
\end{aligned} \tag{5}
$$

Here, e is the electron charge and the parameters I, σ, U'_F, r_s, A, B and C denote the injection current, the cross section area of the active zone, the derivative of the Fermi level separation with respect to n, the series resistivity and the recombination coefficients, respectively. Since all parameters can have different values in different

---

[1]The linear gain $g'(n - n_{tr})$ in Equs. (3,5) can be replaced by the logarithmic model $g' n_{tr} \ln(n/n_{tr})$.

sections (see, e.g., Table 1), the operator H and the rate function $\mathcal{N}$ depend explicitly on the position z. The integration in Equ. (5) is also done within the corresponding section.

3.2 Parameter set

In the sequel we shall illustrate different methods of mode analysis by simulating and analysing the three section laser as represented in Fig. 1a. This laser is completely anti-reflection coated and consists of two DFB (distributed feedback) sections and one phase tuning section integrated in between.

Table 1: Laser parameters used in simulations. φ is a bifurcation parameter.

	explanation	S_1	S_2	S_3	units
c_0/v_{gr}	group velocity factor	3.4	3.4	3.4	
L	length of section	250	400	250	μm
$\kappa^+ = \kappa^-$	coupling coefficient	130	0	130	cm^{-1}
α	internal absorption	25	20	25	cm^{-1}
g'	effective differential gain	9	0	9	10^{-17}cm^2
δ	static detuning (example I)	300	$-\pi/2L_2$	-170	cm^{-1}
	static detuning (example II)	300	$-\varphi/2L_2$	-80	cm^{-1}
α_H	Henry factor	-4		-4	
ε_G	gain compression factor	3		3	10^{-18}cm^{-3}
ε_I	index compression factor	0		0	10^{-18}cm^{-3}
$\bar{g}$	Lorentzian gain amplitude	200	0	200	cm^{-1}
$\bar{\omega}$	gain peak detuning	0		0	ps^{-1}
$2\bar{\gamma}$	FWHM of gain curve	50		50	ps^{-1}
I	current injection (example I)	70		9	mA
	current injection (example II)	70		70	mA
σ	cross-section area of AZ	0.45		0.45	μm^2
U'_F	differential Fermi voltage	5		5	10^{-20}Vcm^3
r_s	series resistivity	5		5	Ω
n_{tr}	transparency carrier density	1		1	10^{18}cm^{-3}
A	inverse carrier life time	0.3		0.3	ps^{-1}
B	bimolecular recombination	1		1	10^{-10}cm^3/s
C	Auger recombination	1		1	10^{-28}cm^6/s
λ_0	central wavelength		1.57		μm
r_0, r_3	facet reflectivity coefficient		0		
r_1, r_2	internal reflectivity coefficient		0		

It is supposed that the two DFB gratings are slightly detuned. The first section (DFB$_1$) is pumped well above threshold and provides gain for lasing. In example I (Sections 4 to 7 of our paper), the second DFB section (DFB$_2$) is driven close to its gain transparency. That is, we have $I \approx e\sigma L R(n_{tr})$ and $n(z,t) \approx n_{tr}$ in this section,

which, therefore, acts as a passive dispersive reflector. In example II (Sections 8 and 9), both DFB sections are pumped above threshold, so that the device is operating as a phase controlled mode beating (PhaseCOMB) laser. The center section has no grating, its active layer does not couple to the laser emission, and, therefore, it serves as a passive phase tuning section. The contribution of this section to the field roundtrip phase is given by

$$\varphi = -2\delta_2 L_2. \tag{6}$$

The parameters belonging to both modi of operation are collected in Table 1. A more detailed discussion concerning fabrication, applicability and numerical simulation of such lasers can be found in [7, 8, 14] and in references therein.

A proper modeling of multisection lasers should take into account nonlinearities. Fortunately, these systems are dissipative, i.e. the solution always approaches an attractor of the system after a more ore less extended transient time. Single-section lasers usually possess only one attractor: a stationary state, i.e. a continuous-wave (cw) emission with stationary carrier densities. In multi-section devices also nonstationary attractors appear like periodic or even chaotic self-pulsations. Furthermore, multiple different attractors may coexist in certain parameter ranges. It depends on the initial conditions, which attractor is approached in these cases. *LDSL-tool* offers different types of initial conditions. Random initial values allow to discover possible multiple attractors in a given point of operation but require in general long transients towards the asymptotically stable solution. Another possibility is to use the final solution of a preceding simulation as initial values for the next one. When changing parameters in sufficiently small steps, the latter procedure yields in general short transients and a smooth continuation of the solution. The nonsmooth transitions between the solutions indicate a bifurcation, where the given attractor changes qualitatively or loses stability. In the following examples, we use this type of initial conditions because it allows to study the dependence of attractors on parameters including their bifurcations.

4   Simulation of a passive dispersive reflector laser

To demonstrate the possibilities of a direct integration of the TW model we first consider the laser structure of Fig. 1a with the parameters labeled 'example I' in Table 1. Here, the third laser section is biased at gain transparency and operates as a passive distributed Bragg reflector. This modus of operation has been successfully used as optical clock in all-optical signal processing at 10 Gbit/s [6]. The behaviour of the device depends sensitively on the contribution of the passive middle section parameter φ (modulo 2π) to the optical round trip phase (see Equ. (6) and Refs. [7, 22]).

Fig. 2 demonstrates the complexity of phenomena obtained by simulation of such a laser when varying the phase parameter φ over one period. At certain values of φ the optical output or / and the carrier density changes qualitatively in an abrupt
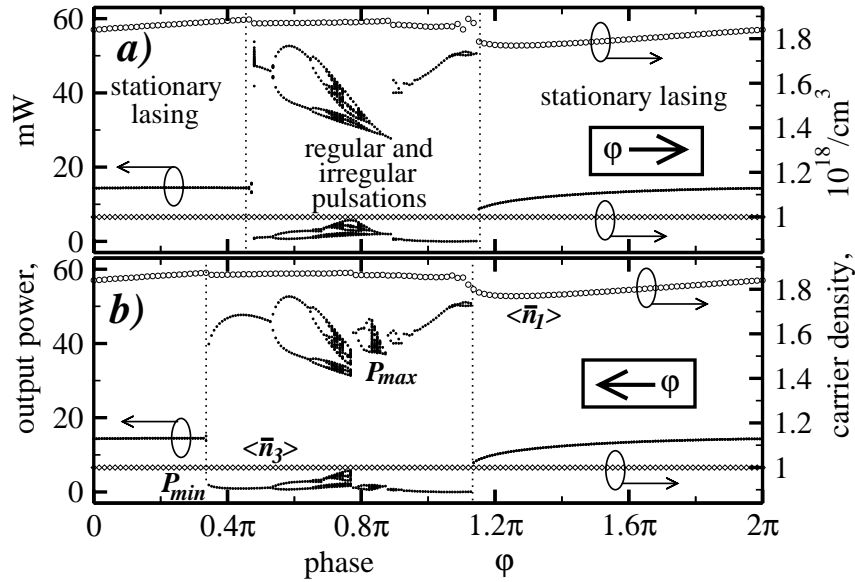
Figure 2: Simulation example I. Panels *a* and *b*: increasing and decreasing, respectively, phase parameter φ. Bullets and diamonds: spatial-temporal averages $\langle \bar{n}_{1,3} \rangle$ of the carrier density in the DFB sections. Dots: relative maxima and minima of the power emitted from the left facet.
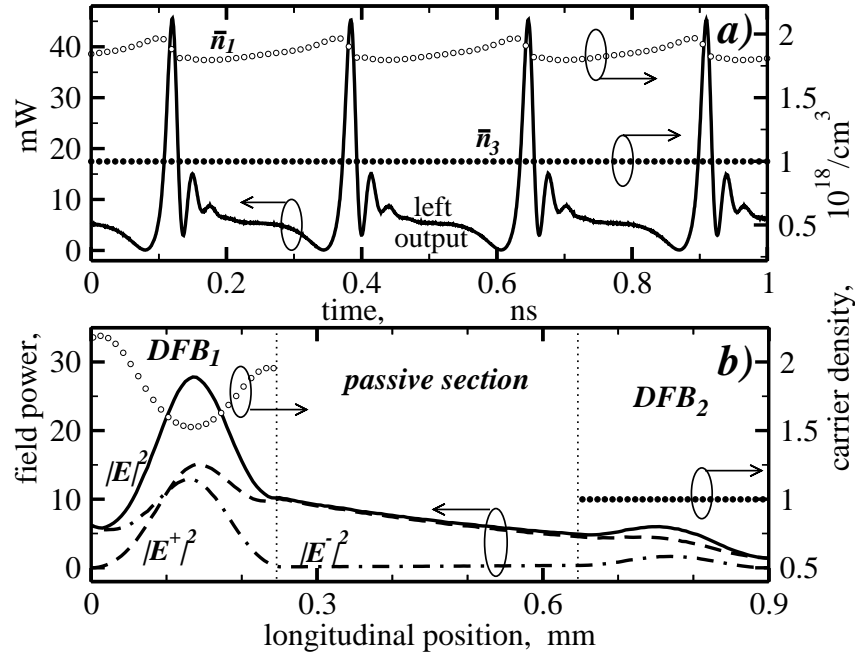

Figure 3: Simulated behaviour of optical fields and carrier densities in a laser at $\varphi = \pi$. Panel *a*: temporal variation. Solid: output from left facet. Empty and full bullets: sectional averages $\bar{n}_{1,3}$ of carrier density within the DFB sections. Panel *b*: axial distributions at the last instant of panel *a*. Dashed: $|E^+|^2$. Dash-dotted: $|E^-|^2$. Solid: total power. Bullets: carrier density.

7

manner. Such bifurcations are a genuine property of nonlinear systems (see, e.g., [16, 23, 24, 25] for a deeper discussion of possible bifurcation scenarios in multisection lasers).

In the given example we tuned φ with small steps, using the final profiles of the functions Ψ and n as the initial values in the simulations at the new step. After finishing the transient regime, the output power maxima and minima and spatio-temporal averages of carrier densities in both DFB sections are recorded. Transitions between different operation regimes are observed at several values of φ. They are different for increasing φ (diagram a) and decreasing φ (diagram b). Obviously, this hysteresis appears because the system approaches different stable long-term solutions in dependence on the initial conditions.

Fig. 2 represents the attractors at different φ by means of only few characteristics. A more detailed characterisation of a self-pulsating solution is given in Fig. 3 for the particular phase $\varphi = \pi$. Panel a of this figure visualises the temporal evolution of the calculated optical output and of the sectionally averaged carrier densities $\bar{n}_1$ and $\bar{n}_3$. The carrier density of section S_3 does not couple to photons and remains nearly constant. The carriers in section S_1 and the optical output show periodic variations. Within each period, the output power exhibits a large first pulse followed by a damped oscillation. This substructure looks like a highly damped relaxation oscillation. However, the frequency of these damped oscillations is about 35 GHz, far beyond typical relaxation oscillation frequencies. Indeed, they are of a completely different nature as the mode analysis below will show.

The axial distribution of powers and carriers at last instant of Fig. 3a is drawn in panel b of the figure. Note the spatial variations of the optical intensity and the carrier density in section S_1. High optical intensity inside this section and corresponding enhancement of the stimulated recombination imply a dip in the carriers. This effect is called spatial hole burning (more details see [14] and Refs. therein).

The examples above show that our model is able to demonstrate a variety of bifurcations as well as nontrivial dynamical regimes possessing spatially nonuniform distributions of fields and carriers. In the following we shall show how many of these effects can be deeper understood when analysing the situation in terms of optical modes.

5　The concept of instantaneous optical modes

Although the concept of modes is basic in laser physics, there exist many different versions depending on the context. In general, the set of optical modes represents all possible natural oscillations of the optical field in a resonator. The standing waves in a usual Fabry-Perot cavity may serve as a well-known example. In the present context, we consider the longitudinal modes of hot multi-section cavities. Mathematically speaking, they are the eigenfunctions and -values of the evolution operator

$H(\beta, z)$ in Equ. (1), i.e. the sets of all complex valued objects $(\Theta(\beta, z), \Omega(\beta))$, which solve the spectral equation

$$H(\beta, z)\Theta(z) = \Omega\Theta(z). \qquad (7)$$

We have explicitly stated that the operator H depends on the actual distribution of $\beta = \beta(z, t)$ along the cavity. Thus, Θ and Ω depend also on this distribution and vary in general with time. They represent the instantaneous mode spectrum of the hot compound cavity. A detailed description of methods used to solve this spectral problem for any fixed distribution of $\beta(z)$ is given in Appendix Section 11.
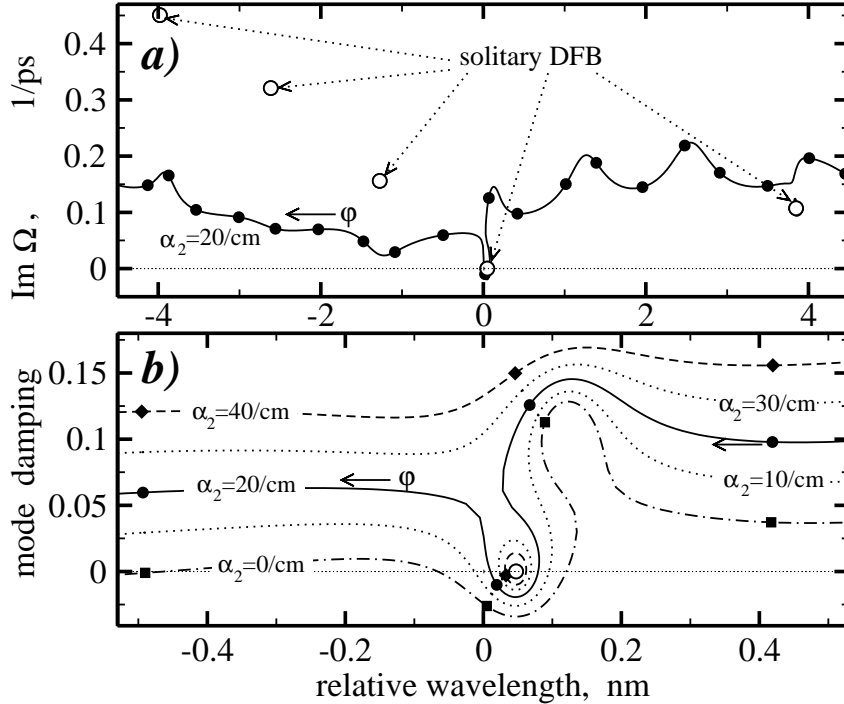

Figure 4: Spectrum of optical modes. Abscissa: relative wavelength $(-\Re e\Omega \cdot \lambda_0^2/2\pi c_0)$. Panel a: overview. Panel b: the modes close to resonance. Lines: location of eigenvalues for all possible φ and different optical losses α_2 in the passive section. Arrows: direction of increasing φ. Full symbols: modes at $\varphi = 0$. Empty bullets: modes of the solitary DFB laser.

For a moment, let us disregard the spontaneous emission noise and consider β not depending on time as in any stationary state of an ideal laser. In this case, $\Psi(z, t) = \exp(i\Omega t)\Theta(\beta, z)$ solves the full TW equation (1). Thus, real and imaginary parts of Ω represent frequency and decay rate of the optical mode, respectively. Fig. 4 shows these quantities for different configurations. First, we have simulated a solitary single-section DFB laser with the parameters of section S_1 as given in the Table 1. Its mode spectrum in case of a stationary operation is shown by the open bullets in Fig. 4. The single mode with $\Im m\Omega = 0$ keeps constant and carries the laser power. All other modes have positive $\Im m\Omega$ and decay if initially present. Their decay rates

9

are very high so that they are damped out within a few picoseconds and play no role even under modulation of the laser in the GHz range.

Now we turn to the full multisection laser. In order to see the impact of the extended cavity, we keep the propagation function β in the DFB_1 section frozen at the solitary laser level, while assuming $n(z) = n_{tr}$ in the remaining sections. Panel a of Fig. 4 shows an increased number of side modes and a general reduction of their decay rates. When tuning the phase parameter φ, these modes are moving along the solid line, each one is replacing its next neighbour after one period.

The scenario close to the fundamental mode of the solitary laser is depicted in Fig. 4b for some fixed values of optical losses α_2 in the passive middle section. In the present example I, the combined second and third sections provide a dispersive delayed feedback of the field back into the active first section. The losses α_2 can be regarded as a measure of the feedback strength. At very low losses (large feedback), all modes are located on a single open curve, exhibiting a deep valley close to the resonance of the solitary laser. When increasing the phase φ, the modes move from right to left through this valley. With increasing losses (decreasing feedback), the valley becomes narrower and deeper. The edges of the valley touch each other at some α_2 between 20 and 30 cm^{-1} forming afterwards an additional closed curve around the fundamental mode of the solitary DFB laser. This loop contains only one mode which is moving around once per phase period. The diameter of the loop shrinks with further increasing losses. At the same time the remaining part of the mode curve shifts upwards, continuously forming new shrinking loops when approaching higher modes of the solitary DFB laser. In the limit of infinite losses, the feedback is zero and all these closed loops collapse into the solitary laser modes.

The simulation example of the previous section corresponds to a middle loss level 20 cm^{-1} (solid line in Fig. 4). A strong dependence of mode damping on φ appears here close to the fundamental mode of the solitary laser. Moreover, at a particular phase value, two neighbour modes located at the opposite valley edges come close to each other. Such a vicinity of two modes is a general indication of a more complex dynamics [26, 27]. Therefore, we turn over now to mode dynamics.

6 Mode expansion of the optical field

In this section we perform a mode analysis of the non-stationary state of the self-pulsating laser simulated in Section 4.

Figs. 5a and 6a present the results of mode computations with the distributions $\beta(z, t)$ calculated along one period of pulsation. Fig. 5a shows the resulting variation of the mode spectrum in the wavelength-damping plane, while Fig. 6a draws the mode damping $\Im m\Omega$ versus time t. Both these diagrams indicate, that the damping of only three or four modes becomes negative or rather small. Accordingly, we expect that only few modes contribute to the dynamics.
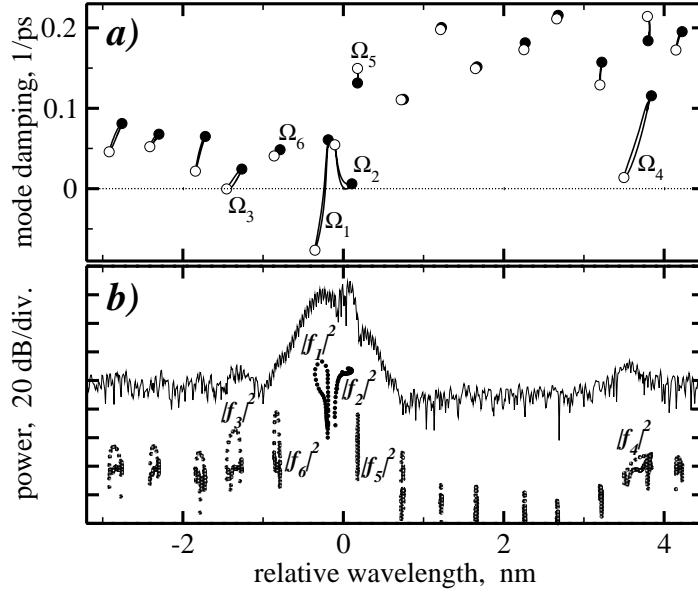
Figure 5: Mode analysis of the pulsating state drawn in Fig. 3a. Panel a: mode spectrum. Empty and full bullets: location of Ω at maximal and minimal sectional average $\bar{n}_1$, respectively. Lines: movement of Ω in between. Panel b: mode decomposition of the optical field. Symbols in lower part: modal contributions $|f_k|^2$ in a series of instants versus modal wavelength. Dots above: optical spectrum of the analysed output field.
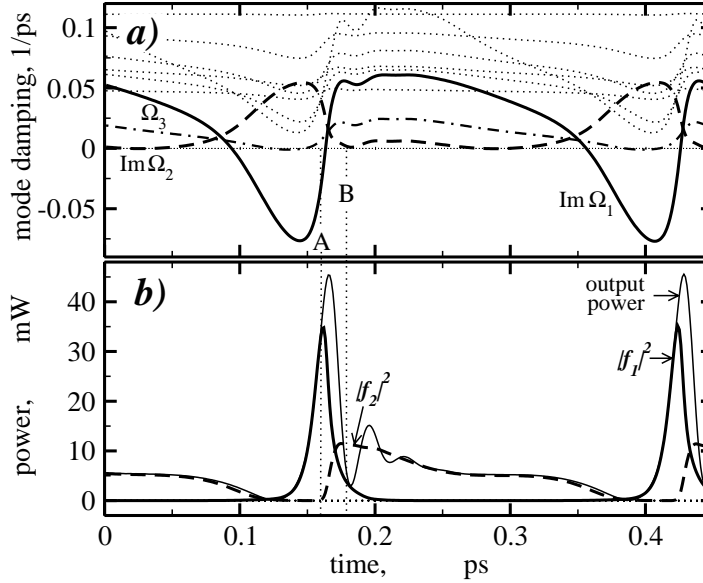

Figure 6: Mode analysis of the pulsating state drawn in Fig. 3a. Panel a: evolution of modal decay rates. Solid, dashed and dash-dotted: modes which sometimes reach zero or negative damping. Thin dotted: modes with always positive damping. Labeling as in Fig. 5. Panel b: evolution of the output field power (thin solid) and modal amplitudes. Solid and dashed bold lines: the two most prominent modal contributions.

11

In order to quantify the different modal contributions, we express the calculated optical state vector $\Psi(z, t)$ at any instant t as a superposition of the instantaneous modes [12, 16]

$$\Psi(z, t) = \sum_{k=1}^{\infty} f_k(t)\Theta^k\left(\beta(z, t), z\right), \tag{8}$$

where the complex modal amplitudes $f_k(t)$ can be calculated as described in the Appendix Section 11. After an appropriate scaling of eigenfunctions $\Theta^k(\beta, z)$, f_k represents the contribution of mode k to the outgoing field E^- at the left facet z_1',

$$E^-(z_1', t) = \sum_{k=1}^{\infty} f_k(t). \tag{9}$$

Figs. 5b and 6b show that only the two modes with labels 1 and 2 are contributing to the analysed dynamical regime while all other modes remain suppressed. These two modes alternate during the pulsation. Mode 1 dominates the first part of the pulses, mode 2 determines the long plateau between them. Beating between them causes damped oscillations of the total intensity which were a puzzling detail of the simulation results. By closer inspecting the behaviour of the two dominating modes we can discover further peculiarities. Firstly, they exhibit a remarkably big variation of the damping rates. Secondly, the damping of mode 2 varies opposite to most other modes. Thirdly, the intensity of mode 2 is steeply rising within a short time interval $[A, B]$ as shown in Fig. 6, although its damping is positive. At the same time, mode 1 starts to decay although still being undamped. These anomalies will be understood in the next section when we will discuss the driving forces for the mode dynamics.

7 Driving forces of mode dynamics

In order to get insight into the different forces causing changes of the modal amplitudes f_k, we substitute the expression (8) into the TW equation (1) and multiply scalarly the resulting equation by the adjoint modes $\Theta^\dagger$ (see the discussion in [21] and Equ. (21) for an explicit expression of $\Theta^\dagger$). Due to the orthogonality of the modes Θ^l and the adjoint modes $\Theta^{k\dagger}$, this procedure yields the following equations of motion for the modal amplitudes:

$$\frac{\partial}{\partial t} f_k = i\Omega_k f_k + \sum_{l=1}^{\infty} K_{kl} f_l + F_k,$$

$$\text{where} \quad K_{kl} \stackrel{def}{=} -\frac{[\Theta^{k\dagger}, \partial_t \Theta^l]}{[\Theta^{k\dagger}, \Theta^k]}, \qquad F_k \stackrel{def}{=} i\frac{[\Theta^{k\dagger}, F_{sp}]}{[\Theta^{k\dagger}, \Theta^k]}, \tag{10}$$

and $[\xi, \zeta]$ denotes the usual scalar product of 4-component complex vector functions. Obviously, the evolution of the amplitude f_k is driven not only by the term with the complex eigenvalues Ω_k. In addition, the second term at the right hand side

of Equ. (10) contains the contributions proportional to the temporal changes $\partial_t \Theta^l$ of the mode functions. The third term in the same formula represents the part of spontaneous emission emitted into mode k. Whereas the first and third terms appear in all types of lasers, the second term is responsible for the peculiarities of the multisection lasers. It describes the redistribution of modal amplitudes due to the changes of the expansion basis. It disappears completely in an ideal single section device with a spatially constant β. In this case only the eigenvalues Ω_k change with β but not the eigenfunctions Θ^k. It can be concluded that the second term in (10) is generally small in well designed single section devices. As a consequence, the amplitudes of different modes evolve independently, each one fed by spontaneous emission.

The situation in multisection devices is different. Variations of β within one section, even if spatially constant there, generally change the β-profile of the whole device. These changes cause variations of the compound cavity modes which in turn imply nonvanishing matrix elements K and their nonnegligible contribution to Equ. (10). Applying the temporal derivative to Equ. (7) and using again the orthogonality of the adjoint modes one can express the corresponding matrix K_{kl} as follows:

$$K_{kl} = \frac{1}{\Omega_k - \Omega_l} \frac{[\Theta^{k\dagger}, (\partial_t H)\Theta^l]}{[\Theta^{k\dagger}, \Theta^k]} \quad (k \neq l), \quad K_{kk} = -\frac{\partial}{\partial t} \ln \sqrt{[\Theta^{k\dagger}, \Theta^k]}. \tag{11}$$

Hence, the coupling term K_{kl} can dominate over the damping term $\Im m \Omega_k$, when the separation $\Omega_k - \Omega_l$ between a mode pair becomes small. This effect is responsible for the growth of mode 2 within the time interval $[A, B]$ in Fig. 6, where its damping term $\Im m \Omega_2$ is still positive. It also explains the early decay of mode 1 within the same interval.

So far we have used Equs. (10) for a deeper understanding of the evolution of the mode amplitudes f_k, which have been determined by the optical state vector $\Psi(z, t)$ and the propagation factor $\beta(z, t)$ obtained in a preceding simulation calculation. Alternatively, it is also possible to combine these equations directly with the carrier equations (2). This yields a set of ordinary differential equations equivalent to the original TW model. By truncating this system to the essential modes and to the essential moments of carrier distributions, one gets an approximate description of the dynamics in a finite dimensional phase space, which also opens the way for a path-following bifurcation analysis. A more detailed description of these mode-approximation techniques together with corresponding examples can be found in, e.g., [15, 16, 22, 23, 24, 26]. For a deeper discussion of the impact of nearly degenerate modes on the dynamics of multisection lasers as well as how to treat the case of degeneracy, we refer to [23, 24, 26, 27].

8   Mode beating pulsations in a PhaseCOMB laser

Let us turn now to example II, the Phase Controlled Mode Beating (PhaseCOMB) regime of operation. Here both DFB sections are pumped above the threshold.

13

Furthermore, the Bragg gratings are detuned by about the stop band width (cf. Fig. 8a) and the two adjacent inner DFB modes are selected for lasing via the phase tuning in the middle section. Beating of the two coupled modes leads to self-pulsations with a frequency determined by the spectral separation of the lasing modes [8, 26]. Practical realizations of this regime up to 80 GHz and its application in optical signal processing have been reported (e.g., [17]).

Simulation calculation Fig. 7 characterises a typical self-pulsating state calculated for the phase parameter $\varphi = \pi$. Both DFB sections contain comparably high carrier densities and optical powers (panel b), they operate above the laser threshold. The emitted power (panel a) exhibits well modulated nearly sinusoidal oscillations with about 70 GHz frequency. The carrier densities are extremely weakly modulated with the same frequency.
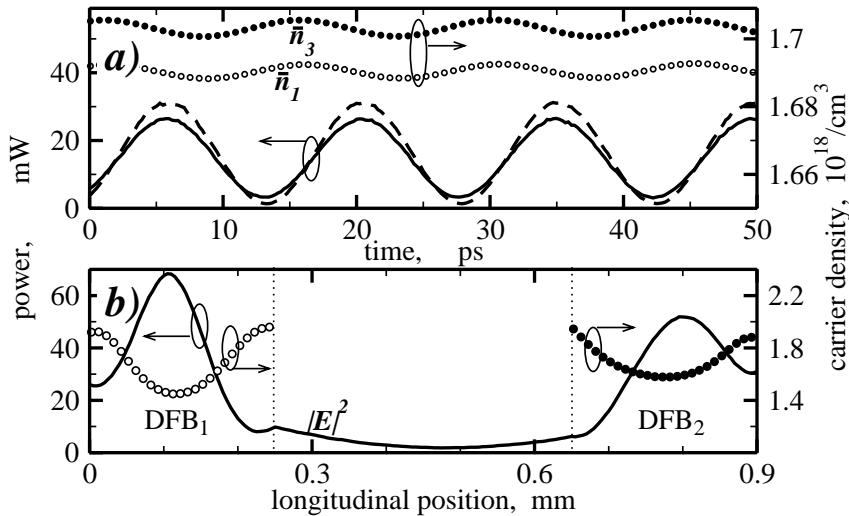

Figure 7: Simulated behaviour of optical fields and carriers in the PhaseCOMB laser at $\varphi = \pi$. Diagrams and notations as in Fig. 3. The dashed line in panel a is the output power at the right facet.

Mode decomposition The motion of the eigenvalues during one pulsation period is shown in Fig. 8c. It is smaller than the symbol size in accordance with the weak carrier modulation and in contrast to Fig. 3a of example I. The two lowest modes (labeled 1 and 2) have zero damping level, i.e., both they are at threshold. Their expansion coefficients (panel d) are comparable, they exceed those of all other modes by orders of magnitude and represent well the two major peaks in the optical spectrum. We conclude that the self-pulsating state is carried by two modes lasing at the same time.

The spectral position of the two major modes agrees fairly well with the two adjacent inner resonance peaks of the reflectivity spectra of the DFB sections calculated in the given state of operation (panel a). Thus, each mode of this pair can be attributed to

14

one of the two DFB sections. This conclusion is supported by the coinciding spectral positions of the modes of isolated DFB sections with the same carrier densities (open symbols in panel c).
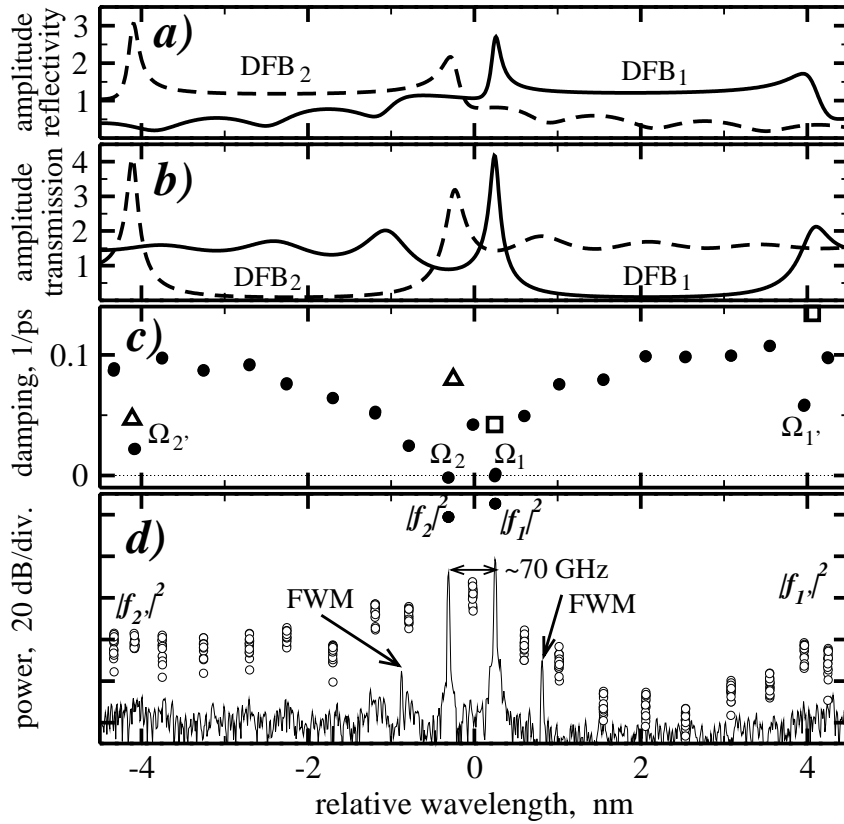

Figure 8: Mode analysis of the pulsating state drawn in Fig. 7. Panels a and b: reflectivity and transmission spectra of DFB_1 (solid) and DFB_2 (dashed) sections; Panel c: mode spectrum of the PhaseCOMB laser (bullets). The mode spectra of noncoupled solitary DFB_1 (squares) and DFB_2 (triangles) sections are given for comparison. Panel d: optical spectra of the emission from the left facet (thin line) and modal contributions $|f_k|^2$ versus modal wavelength (bullets).

The higher damping of these solitary DFB laser modes on the other hand indicates an important role of the interaction between both DFB sections in the self-pulsating state. To a certain extend, the strength of this interaction can be represented by the reflectivity of the corresponding opposite DFB section. These reflectivities are rather high over a wide spectral range (panel a). Thus, this useful interaction is accompanied by the formation of a Fabry-Perot like cavity, which gives rise to the comb of only moderately damped side modes in panels c and d.

The calculated optical spectrum in panel d exhibits a few additional side peaks, which are small but well above the noise background. Similar features have been detected in experimental spectra. It seems to be obvious to attribute them to weekly damped side modes. However, the mode decomposition yields: there is no side mode at the position of the most prominent side peak. The real cause of these peaks is

15

the four-wave mixing (FWM) of the two main modes. The presence of FWM-peaks is generally an indication of a good overlap of the two waves and of their nonlinear interaction.

Spatio-temporal properties of mode-beating self-pulsations The results of the mode analysis presented above allow a deeper insight into the spatio-temporal behaviour of the fields within the self-pulsating laser. Two modes $k = 1, 2$ dominate the expansion (8). The corresponding eigenvalues $\Omega_k(t)$ and eigenfunctions $\Theta^k(z, t)$ vary extremely weakly around their means $\bar{\Omega}_k$ and $\bar{\Theta}^k(z)$. Thus it holds

$$f_k(t) \approx f_k(0) \exp(i\omega_k t), \qquad\qquad k = 1, 2,$$

where $\omega_k = \Re e \bar{\Omega}_k$ is the mean modal frequency. The intensities of both the forward and the backward travelling wave within the laser are well approximated by

$$P(z, t) \quad \approx \quad |E_1(z)|^2 + |E_2(z)|^2 + 2|E_1(z)||E_2(z)| \cos\left(\Delta\omega\, t - \phi(z)\right). \quad (12)$$

Here,

$$E_k(z) \stackrel{def}{=} f_k(0)\bar{\Theta}^k_E(z), \quad \Delta\omega \stackrel{def}{=} \omega_2 - \omega_1, \quad \phi(z) \stackrel{def}{=} \arg(E_2(z)) - \arg(E_1(z))$$

are the initial optical mode amplitudes, the mean frequency difference between the two dominant modes, and the initial mode phase difference, respectively. Superscripts $\pm$ distinguishing between forward and backward are omitted for simplicity. All expressions hold for the both propagation directions.

The axial distributions of the amplitudes $|E_k(z)|$ and the phase difference $\phi(z)$ are drawn in Fig. 9 for the particular pulsation under consideration. Although the two modes originate from different DFB sections, their amplitudes are comparable over all the compound cavity. Thus, the beating term in Equ. (12) causes everywhere a considerable modulation of the optical intensity, which in turn drives the carrier oscillations in the active sections.

Practical applications of self-pulsating lasers usually require a good extinction of the pulses, i.e., the outgoing amplitudes of both modes at the given facet should be comparable. In our example, this condition is best achieved at the right facet (open squares in Fig. 9). In this context it is important that the section DFB$_2$ supports not only its own mode 2 but also amplifies the wave of mode 1. The corresponding transmission depends strongly on the wavelength (Fig. 8b). It becomes very small if the two stop bands overlap too much. Thus, one should avoid this situation by properly adjusting the detuning of the DFB gratings in order to get self-pulsations with a high extinction.

The axial variation of the phase difference $\phi(z)$ between the two modes plays also an important role. It is a general rule that the corresponding phase difference between any two neighbouring modes k and $k+1$ $(\omega_{k+1} > \omega_k)$ increases exactly by 2π over one round trip in propagation direction. In the present example, it increases by 4π
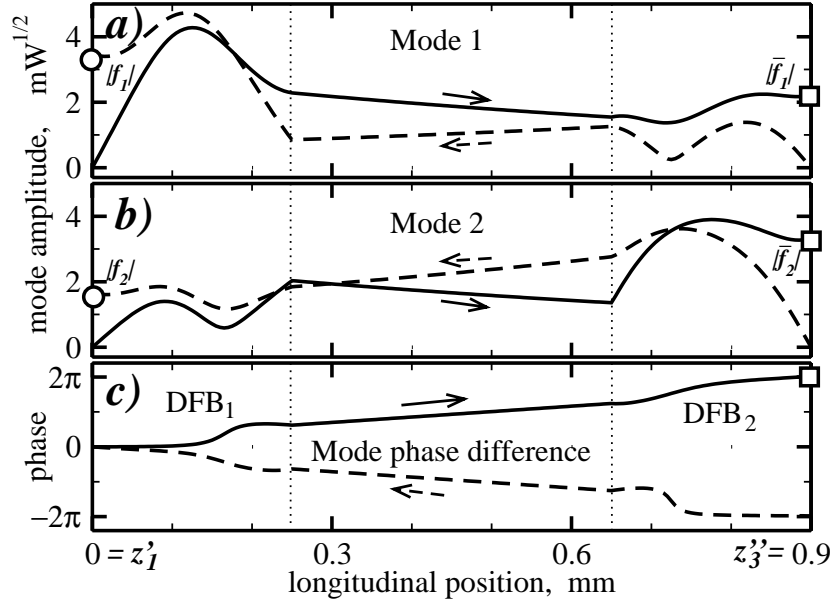
16

Figure 9: Axial mode structure. Panels a and b: forward and backward traveling amplitudes $|E_k(z)|$ of the two main modes of Fig. 8. Panel c: phase differences $\phi(z)$ between them. Forward and backward propagating parts are given by solid and dashed lines, respectively. The open symbols indicate the amplitudes of mode waves emitted from the facets.

(see line separation at the right facet z_3'' in Fig. 9c) because we have one weak mode between the two dominant ones.

Due to the increasing phase difference, the peak of the beating pulse travels cyclic around the cavity. A similar behaviour is known from mode locked Fabry-Perot lasers. However, pulse speed and pulse length are very different in both cases. In a mode-locked laser the speed equals the constant group velocity v_{gr}, the multi-mode pulses are very short and the length of the laser determines the repetition rate $v_{gr}/2L$. In our devices, the pulse peaks travel with v_{gr} only in the passive middle section, the two-mode pulses are nearly sinusoidal and the frequency difference $\Delta\omega$ determining the repetition rate is impressed by the grating detuning but not by the device length.

Due to the high symmetry of our device, the single pass phase shift is nearly half the round trip phase shift, i.e. 2π in our case. This explains the in-phase oscillations of both emitted powers shown in Fig. 7a. At variance, anti-phase will appear if the dominant modes are neighbouring or have an even number of modes in between.

9 Phase control of mode-beating pulsations

After the detailed study of the particular case $\varphi = \pi$ in the previous section, we shall briefly sketch the use of mode analysis for understanding switchings between

17

qualitatively different types of mode-beating pulsations. In particular, we control these regimes by tuning the phase parameter φ.

Simulation of phase tuning   First we report on simulation calculations for both increasing and decreasing φ. The method of calculations is the same as already explicated in connection with Fig. 2. Selected results are summarized in panels a and b of Fig. 10. Obvious bifurcations appear at the positions B, D, and F when tuning φ in forward direction and at E, C, and A when tuning φ backward. Accordingly, at least two attractors coexist in the regions $[A, B]$, $[C, D]$, and $[E, F]$. Unique pulsating states are observed within the rest of the phase period.

Mode analysis   It is not possible to give here a complete description of all phenomena observed in the simulation. Therefore, we confine the mode analysis to the case of increasing phase φ. Wavelengths and dampings of a few modes calculated in accidentally chosen instants t are presented in panels c and d, respectively. We did not determine mean values because the extremely weak oscillations of $\beta(z)$ usually imply accordingly small variations of the modes.

The mode system as a whole is 2π periodic in φ. However, the wavelength of each individual mode shifts down with φ and every mode arrives at the position of its former next neighbour after one period. As an example, the dominant modes 1_n, 2_n, and $2'_n$ at $\varphi = 2\pi$ are identical with modes 1, 2 or 2' dominating at $\varphi = 0$. Consequently, at least one discontinuous jump of each operating mode must appear within every phase tuning period.

Regimes of operation   The pulsations with ~ 70 GHz frequency within the phase interval $[D, F]$ are determined by the two second-neighbour modes 1_n (grey bullet) and 2_n (black square). The damping of both these modes is practically zero. This case has been already extensively described in the previous section.

In the range $[B, D]$, the situation is a bit different. In connection with highly asymmetric carrier densities, the two closest neighbour modes 1 (open rhombi) and 2_n (black squares) are dominating here. They drive pulsations of only ~ 30 GHz frequency. Surprisingly, the dampings of the two dominant modes differ now considerably from zero and exhibit a large scatter. The reasons are as follows. The smaller mode separation implies an increase of the mode coupling factor K, which allows a larger deviation of the main mode damping factors $\Im m\Omega$ from zero (see Equs. (10,11) and the discussion in Section 7). This increased coupling gives also rise to higher FWM peaks (panel c). Moreover, the lower frequency causes stronger modulations of the β-distribution and, in turn, a more significant shift of some modes during pulsations. These deeper modulations are also responsible for the scatter of mode dampings (interval $[B, D]$ in panel d) calculated at arbitrary instants during the pulsations.

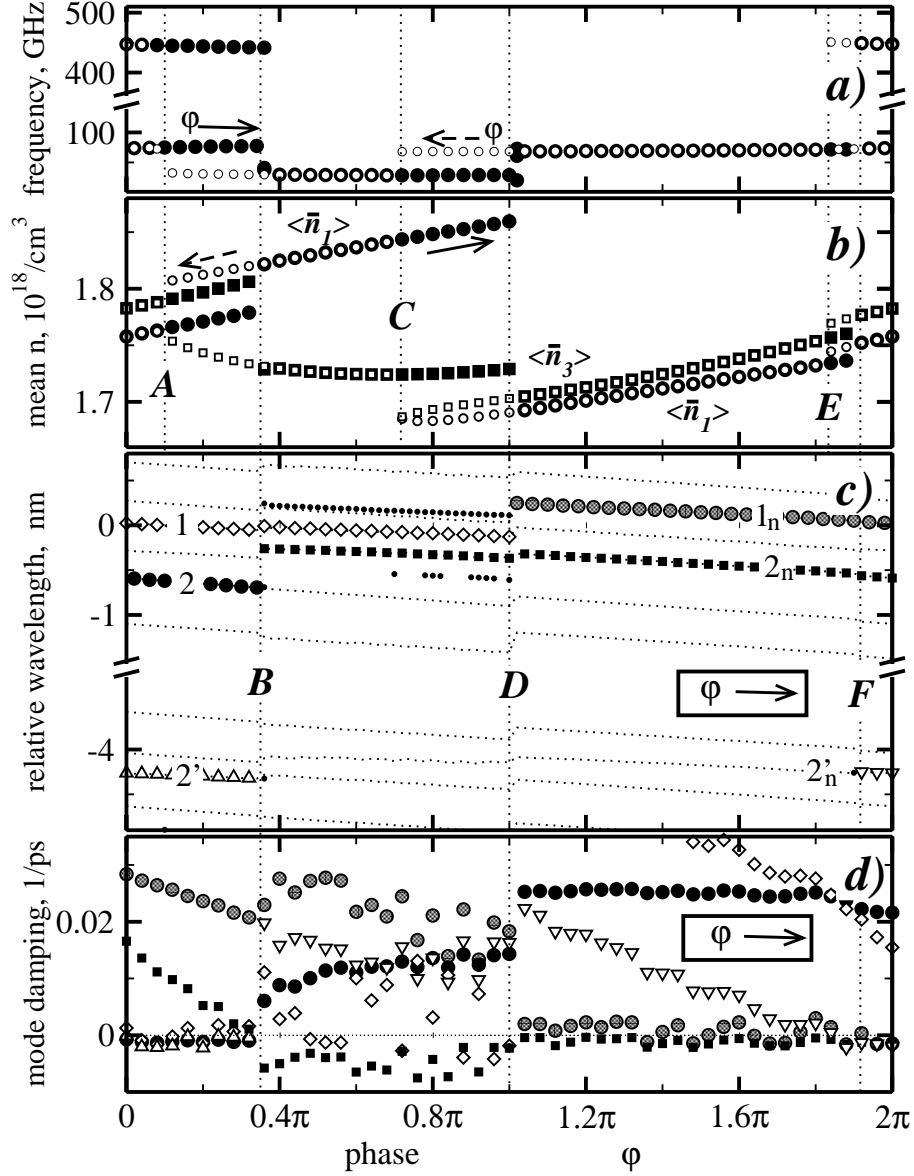Within the phase interval $[F, 2\pi]$ continued in $[0, B]$, three modes are dominating

Figure 10: Phase tuning characteristics of a PhaseCOMB laser. Panels *a* and *b*: simulation calculations for decreasing (empty symbols) and increasing (full symbols) phase φ. Panel *a*: frequencies of the dominant peaks in the rf power spectrum (left facet); only side peaks suppressed by $\leq 10\text{dB}$ are considered. Panel *b*: spatio-temporal averages of carrier densities in DFB_1 (bullets) and DFB_2 (squares). Panel *c*: wavelengths of all modes in the given spectral range (dotted lines). Big symbols indicate positions of dominant peaks (differing by $\leq 10\text{dB}$). The medium symbols in interval $[B, D]$ represent four-wave mixing side peaks, which are suppressed by $\leq 40\text{dB}$ here. Panel *d*: damping $\Im m\Omega$ of important modes. The same symbols as in panel *c* are used but side modes are also shown.

19

simultaneously. Their damping is close to zero at the same time (panel d). This cooperation of 3 modes with comparable intensities causes three large peaks in the optical spectrum (panel c) and two peaks at about 70 and 450 GHz in the rf power spectrum (panel a). In contrast to the previous cases, now the DFB$_2$ section is simultaneously supporting different stopband side modes 2 and 2′. It seems that this robust operation of three modes is possible only due to the nonuniform distribution of carriers within DFB sections: while spatial hole burning within DFB$_2$ tends to select mode 2′, the slightly stronger coupling between modes 1 and 2 due to the larger factor K in Equs. (10,11) allows to support mode 2 as well. A deeper analysis of this interesting case is however beyond the scope of this presentation.

Bifurcations   Let us discuss now the mode analysis nearby the bifurcations. For brevity we consider only bifurcation positions B and F. Panel b shows a general increase of the mean carrier densities in both DFB sections when approaching these bifurcations from left. The corresponding higher gain is required to keep the respective dominant modes at threshold, although the phase condition becomes increasingly bad for these modes. In both cases, the increasing gain causes also a gradual decrease of the damping of one side mode. The bifurcation appears when this side mode becomes undamped.

The bifurcation at the position B is accompanied by a sudden redistribution of the carriers. As a result, two formerly dominant modes become damped and a new dominant mode takes over. On contrary, the change of carrier distributions is small at the position F. The system of dominant modes is only supplemented by an additional member, that mode whose damping approached to zero.

The scenarios of the other transitions between pulsating states are more complicated. Their analysis requires additional considerations which are beyond the scope of this paper.

10   Conclusion

In this work we discuss and demonstrate the possibilities of the software *LDSL-tool* studying the longitudinal mode dynamics. Computation of modes, decomposition of non-stationary field into modal components, study of the mode spectra, of the relations and different transitions between modes and the mode dependencies on different parameters allow to achieve deep understanding of the processes observed in direct integration of model equations as well as in experiments.

11   Appendix: Numerical methods

In this section we give a derivation of some formulas and introduce briefly the numerical methods used to solve the problems discussed above.

11.1 Numerical integration of model equations

There is a variety of numerical methods to integrate different forms of the TW model (1,2). Examples are the transfer matrix method [20, 28], the power matrix method [29], finite difference schemes [10], the split step method [30], and the transmission line method [31]. These approaches do not use polarization equations but introduce dispersion effects by means of digital filter techniques. We prefer the polarisation model because it yields a well defined analytic description of the field evolution operator $H(\beta, z)$ which we analyzed along this work.

The numerical integration of the partial differential TW equations is mostly based on the field propagation in time and space along characteristic directions ($v_{gr}t \pm z =$ const) determined by the group velocity v_g. This approach is also used in our work, where we treat the equations for the fields $E^{\pm}$ by means of second order accuracy central finite difference schemes. The ordinary differential equations for the polarisations $p^{\pm}$ as well as for the carrier densities n are integrated by means of central finite difference schemes.

Discretization of the domain The continuous functions $E(z,t)$, $p(z,t)$ and $n(z,t)$ are approximated by their discrete analogues. The values of such grid functions are determined on section-wise uniform temporal-spatial meshes represented schematically in Fig. 11.
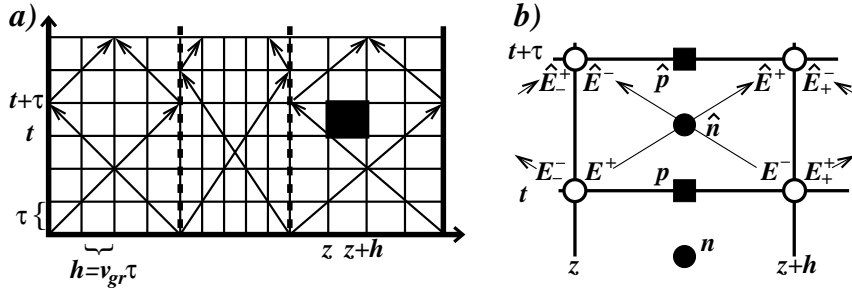

Figure 11: Discretization of the spatial-temporal domain. Panel *a*: full domain overview. Panel *b*: positions (solid symbols) where grid functions are defined and their notations in the neighbourhood of one cell (black box in panel *a* of this figure) of the mesh.

To generate the mesh for grid function E of the optical field, we discretize the time axis with a uniform step τ (horizontal thin lines). This time step should be sufficiently small in order to cover a required optical frequency range $\mathcal{F}$: $\tau \le 1/\mathcal{F}$. The spatial axis is discretized with uniform steps $h = v_{gr}\tau$ (vertical thin lines). Junctions between sections should contain mesh points. Therefore, it is supposed that the length of each section is an integer multiple of $v_{gr}\tau$. The diagonal points of this mesh are located along the characteristic directions of the TW equations (slant arrows) in accordance with the physical field propagation. From the point of view of numerical analysis, such discretization is able to support a stable and convergent

numerical scheme. Finally, the grid polarization and grid carrier density functions are considered on the meshes shifted by $h/2$ and $(h/2, \tau/2)$, respectively.

Numerical schemes Let E, $E_\pm$, $\hat{E}$ and $\hat{E}_\pm$ denote the grid field function values at the neighbouring mesh points indicated by empty bullets in panel b of Fig. 11. Similarly, by p, $\hat{p}$, n and $\hat{n}$ we denote grid polarization and carrier density function values at the positions denoted by full bullets and squares in the same figure.

Assume we know the values of grid function n (at the time layer $t - \tau/2$) and $E^\pm$, $p^\pm$ (at the time layer t). The grid function $\hat{n}$ is a solution of the finite difference scheme approximating Equ. (2) at the positions $(z + h/2, t)$:

$$\frac{\hat{n} - n}{\tau} = \mathcal{N}\left(\frac{\hat{n} + n}{2}, P, P_p, z + \frac{h}{2}\right),$$
$$P \stackrel{def}{=} \sum_{\nu=\pm} \frac{|E^\nu|^2 + |E^\nu_\nu|^2}{2}, \qquad P_p \stackrel{def}{=} \Re e \sum_{\nu=\pm} \frac{(E^\nu + E^\nu_\nu)^* p^\nu}{2}. \tag{13}$$

The integral term used in the definition of the function $\mathcal{N}$ should be replaced by the sectional average of the corresponding grid carrier density function.

To find the grid functions $\hat{E}^\pm$ and $\hat{p}^\pm$, we are solving the difference schemes approximating Equ. (1) at the positions $(z + h/2, t + \tau/2)$:

$$\frac{\hat{E}^\pm - E^\pm}{h} = -\left(i\beta(\hat{n}, \tilde{P}) + \frac{\bar{g}}{2}\right)\frac{\hat{E}^\pm + E^\pm}{2} - i\kappa^\mp \frac{\hat{E}^\mp + E^\mp}{2} + \frac{\bar{g}}{2}\frac{\hat{p}^\pm + p^\pm}{2},$$
$$\frac{\hat{p}^\pm - p^\pm}{\tau} = \bar{\gamma}\frac{\hat{E}^\pm + E^\pm}{2} + (i\bar{\omega} - \bar{\gamma})\frac{\hat{p}^\pm + p^\pm}{2}, \quad \tilde{P} \stackrel{def}{=} \sum_{\nu=\pm} \frac{|\hat{E}^\nu|^2 + |E^\nu|^2}{2}. \tag{14}$$

In addition, at the edges of sections, the grid optical field functions $\hat{E}^\pm$ are satisfying the boundary-junction conditions given in Equ. (4). In the case of nonzero spontaneous emission (i.e., $F_{sp}^\pm \neq 0$), we add properly normalized uncorrelated complex random numbers to the newly found optical fields $\hat{E}^\pm$ at each spatial grid point.

The scheme (13) is, in general, nonlinear with respect to $\hat{n}$ and is resolved by an iterative procedure. The already computed grid function n is used as initial approximation for $\hat{n}$ in the nonlinear terms and in sectional averages. Since the carrier density varies slowly, a single iteration step is sufficient here to get a good approximation of $\hat{n}$. A similar procedure is used to resolve the schemes (4,14) for the optical fields in cases $\varepsilon_{G,I} \neq 0$, i.e., when β is effectively dependent on the photon density $\tilde{P}$.

11.2   Computation of modes

The vector-function $\Theta(\beta, z)$ can be splited into field $\Theta_E = (\Theta_E^+, \Theta_E^-)^T$ and polarization $\Theta_p = (\Theta_p^+, \Theta_p^-)^T$ parts. The spectral problem (7) together with the boundary

conditions (4) can be written as

$$
\begin{cases}
H_0(D,z)\Theta_E(\beta,z) = 0, \quad D(\beta,\Omega) \stackrel{def}{=} \beta + \frac{\Omega}{v_{gr}} - \frac{i\bar{g}}{2}\frac{i(\Omega-\bar{\omega})}{\bar{\gamma}+i(\Omega-\bar{\omega})}; \\
\Theta_E(\beta,z) \quad \text{satisfy (4);} \qquad \text{scaling: } \Theta_E^-(\beta,z_1') = 1; \\
\Theta_p(\beta,z) = \frac{\bar{\gamma}}{\bar{\gamma}+i(\Omega-\bar{\omega})}\,\Theta_E(\beta,z).
\end{cases}
\tag{15}
$$

This system should be considered separately in each laser section.

Transfer matrices and characteristic function   Assume that β and Ω are fixed and we know the the value of function Θ_E at the left edge z_k' of the section S_k. To find the function $\Theta_E(\beta,z)$ at any other z of the same section, we need to solve a system of ODE's (given by the first line of Equ. (15)) in this section. For β and κ constant within S_k, the solution of this linear problem is given by transfer matrices M_k^S:[2]

$$
\begin{aligned}
\Theta_E(\beta,z) &= \begin{pmatrix} \cos\eta - \frac{iD_k(z-z_k')}{\eta}\sin\eta & -\frac{i\kappa_k^-(z-z_k')}{\eta}\sin\eta \\ \frac{i\kappa_k^+(z-z_k')}{\eta}\sin\eta & \cos\eta + \frac{iD_k(z-z_k')}{\eta}\sin\eta \end{pmatrix} \Theta_E(\beta,z_k') \\
&\stackrel{def}{=} M_k^S(z,\beta,\Omega)\Theta_E(\beta,z_k'); \quad \eta \stackrel{def}{=} (z-z_k')\sqrt{D_k^2 - \kappa_k^+\kappa_k^-} \in \mathbf{C}.
\end{aligned}
\tag{16}
$$

Boundary-junction conditions (4) and the scaling of Θ imply the following conditions on the eigenfunction $\Theta_E(\beta,z)$ at the edges of laser sections:

$$
\begin{aligned}
\Theta_E(z_{k+1}') &= \frac{1}{t_k}\begin{pmatrix} 1 & -r_k^* \\ -r_k & 1 \end{pmatrix}\Theta_E(z_k'') \stackrel{def}{=} M_k^J\Theta_E(z_k''), \quad 0 < k < m; \\
\Theta_E(z_1') &= \begin{pmatrix} -r_0^* \\ 1 \end{pmatrix}, \qquad \Theta_E(z_m'') = c\begin{pmatrix} 1 \\ r_m \end{pmatrix}, \qquad c \in \mathbf{C}.
\end{aligned}
\tag{17}
$$

Here the transfer matrices M_k^J show how the functions $\Theta_E(\beta,z)$ are propagated through the junction of the sections S_k and S_{k+1}.

We know now, how the function Θ_E is transfered through sections and junctions of the sections. Thus, the consequent multiplication of the matrices M^S and M^J allows us to construct an overall transfer matrix $M(z,\beta,\Omega)$ determining the propagation of Θ_E from the left facet of the laser z_1' to an arbitrary position z. Moreover, the assumed scaling of Θ (known value of $\Theta_E(\beta,z_1')$) together with the easy relation between Θ_p and Θ_E (as given in Equ. (15)) allows to determine completely the eigenfunction $\Theta(\beta,z)$ for arbitrary $z \in S_k$:

$$
\begin{aligned}
\Theta_E(\beta,z) &= M_k^S(z)\Big[M_{k-1}^J M_{k-1}^S(z_{k-1}'') \cdots M_1^J M_1^S(z_1'')\Big]\begin{pmatrix} -r_0^* \\ 1 \end{pmatrix} \\
&\stackrel{def}{=} M(z,\beta,\Omega)\begin{pmatrix} -r_0^* \\ 1 \end{pmatrix}; \quad \Theta_p(\beta,z) = \frac{\bar{\gamma}}{\bar{\gamma}+i(\Omega-\bar{\omega})}\Theta_E(\beta,z).
\end{aligned}
\tag{18}
$$

---

[2] For nonuniform β or κ within S_k we find the transfer matrices in small subintervals between z_k' and z where β or κ are approximated by constants. These subintervals can correspond to the spatial steps of the numerical scheme. The product of these matrices of all subintervals gives an approximation of required transfer matrix.

The value of the vector function Θ_E at the right facet z_m'' of the laser can be defined by means of the transfer matrix $M(z_m'', \beta, \Omega)$ or immediately taken from Equ. (17). The equality of these complex two-component vectors implies a complex algebraic *characteristic equation*

$$\mathcal{M}(\Omega; \beta) \overset{def}{=} (-r_m, 1) M(z_m'', \beta, \Omega) \begin{pmatrix} -r_0^* \\ 1 \end{pmatrix} = 0, \tag{19}$$

where $\mathcal{M}(\Omega; \beta)$ is a nonlinear complex algebraic *characteristic function* of the complex variable Ω. Here β is fixed and is treated as a parameter. The set of complex roots Ω of this function coincides with the set of eigenvalues of the original spectral problem. With any Ω satisfying Equ. (19), one can easily reconstruct the corresponding eigenfunction Θ by means of Equ. (18). Thus, in order to solve the spectral problem we are looking for the roots of the function $\mathcal{M}(\Omega; \beta)$ which is analytic in all complex domain with exception of some singular points.

Finding roots of the characteristic equation The complex equation (19) has an infinite number of roots which, in general, need not to be isolated [23, 27]. Among these roots we are looking for a finite number of those with low damping (negative or small positive $\Im m \Omega$) and $\Re e \Omega$ from some certain frequency range. For simplicity, we assume that the derivative $\partial_\Omega \mathcal{M}$ computed at these roots remains nonzero, i.e., these roots remain isolated from each other.[3] To find the roots Ω_r, $r = 1, \ldots, q$ we apply Newton's iteration scheme

$$\Omega_{r(j+1)} = \Omega_{r(j)} - \mathcal{M}(\Omega_{r(j)}; \beta) \big/ \partial_\Omega \mathcal{M}(\Omega_{r(j)}; \beta), \qquad j \to \infty. \tag{20}$$

Here $\{\Omega_{r(j)}\}_{j=0}^\infty$ is a sequence of approximations converging rapidly to Ω_r, if only the factor $|\partial_\Omega \mathcal{M}(\Omega_{r(j)}; \beta)|$ is not too small.

The initial approximation $\Omega_{r(0)}$ is determined by parameter continuation (homotopy method) from known previous solutions for a similar laser with the same length and the same number of sections. The parameters are changed in small steps towards the parameter set of the actual laser and the Newton's iteration scheme is applied in each step. The step size is chosen inversely proportional to the maximal distance between corresponding roots of the previous two steps. This step adjustment allows to guarantee a good initial approximation for Newton's scheme at the next parameter step.

If suitable previous solutions are not available, we start the parameter continuation from a Fabry-Perot type laser ($\kappa^\pm = \bar{g} = 0$, $r_j = 0$ for $0 < j < m$ and $r_0 = r_m = 1$). In this case the related transfer matrix M has a simple diagonal form and all roots of the characteristic function can be written explicitly:[4]

$$\Omega_r = \left(\pi r + \frac{\pi}{2} - \sum_{k=1}^m \beta_k L_k \right) \Big/ \left(\sum_{k=1}^m L_k / v_{gr,k} \right), \qquad r \in \mathbf{N}.$$

---

[3]Mode degeneracy appears only at singular parameter constellations. The very proximity to it modifies however the laser dynamics [24, 26].

[4]Besides these roots, the characteristic function with $\bar{g} \neq 0$ has still an infinite number of roots concentrated nearby to $\bar{\omega}_k + i\bar{\gamma}_k$, $k = 1, \ldots, m$ (see [23]). Until $\bar{\gamma}$ are large enough, the impact of these "polarization modes" can be neglected.
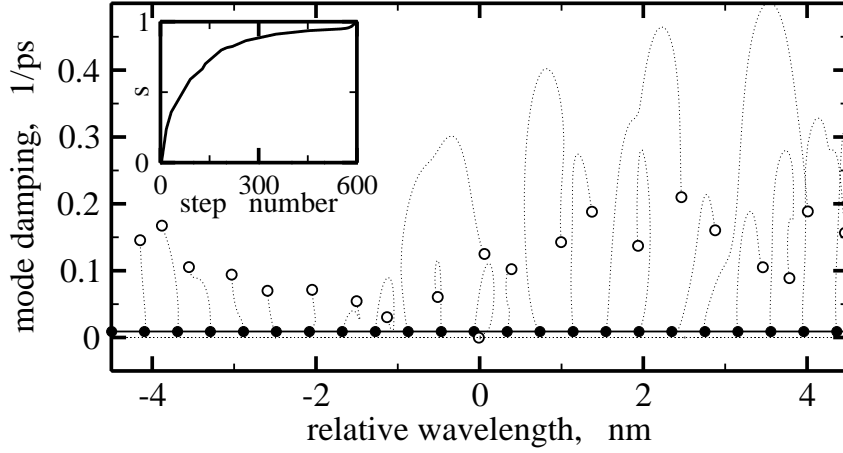
Figure 12: Evolution of modes during parameter continuation from a simple Fabry-Perot type laser (full bullets, $s = 0$) towards the 3 section DFB laser of Example I (empty bullets, $s = 1$). Insert: relative distance s from the initial parameter set versus step number.

Evolution of modes from these values during parameter continuation is illustrated in Fig. 12.

11.3 Mode decomposition

Assume we have computed the functions $E(z,t)$ and $p(z,t)$ in a given instant t. Using also computed distribution $\beta(z,t)$ and following Equ. (18) we find q eigenfunctions $\Theta(\beta(z,t),z)$. The corresponding eigenfunctions $\Theta^\dagger$ of the adjoint problem read as

$$\Theta^\dagger(\beta,z) = \begin{pmatrix} \Theta_E^\dagger(\beta,z) \\ \Theta_p^\dagger(\beta,z) \end{pmatrix} = \left(\Theta_E^{-*}, \Theta_E^{+*}, \frac{v_{gr}\bar{g}}{2\bar{\gamma}}\Theta_p^{-*}, \frac{v_{gr}\bar{g}}{2\bar{\gamma}}\Theta_p^{+*} \right)^T. \tag{21}$$

Exploiting the orthogonality of Θ and $\Theta^\dagger$, we find the modal amplitudes $f_k(t)$ appearing in Equ. (8):

$$f_k(t) = \left[\Theta^{k\dagger}(\beta(z,t),z), \begin{pmatrix} E(z,t) \\ p(z,t) \end{pmatrix} \right] \Big/ \left[\Theta^{k\dagger}(\beta(z,t),z), \Theta^k(\beta(z,t),z) \right].$$

To estimate the scalar product of the grid functions E and p with the analytically given eigenfunction $\Theta^{k\dagger}$ we use the trapezoidal rule for approximate integration. The scalar product in the denominator is given by the analytic formula[5]

$$\begin{aligned}
\left[\Theta^\dagger, \Theta \right] &= \sum_{r=1}^m \left(1 + \frac{v_{gr,r}\bar{g}_r\bar{\gamma}_r}{2(\bar{\gamma}_r + i(\Omega - \bar{\omega}_r))^2} \right) \frac{i\left[\kappa_r^- \Theta_E^{-2} - \kappa_r^+ \Theta_E^{+2} \right]\big|_{z_r'}^{z_r''} + \chi_r}{2(D_r^2(\Omega) - \kappa_r^+\kappa_r^-)}, \\
\chi_r &\stackrel{def}{=} 2D_r(\Omega)L_r[2D_r(\Omega)\Theta_E^+\Theta_E^- + \kappa_r^-\Theta_E^{-2} + \kappa_r^+\Theta_E^{+2}]\big|_{z_r'}.
\end{aligned}$$

---

[5]We assume that β is constant in each section. If not, we split the sections into smaller subsections where β can be treated as constant and use again this formula.

25

$D(\Omega)$ is defined in Equ. (16), $\Theta_E^\pm$ at the section edges z_r' and z_r'' is found from formula (18).
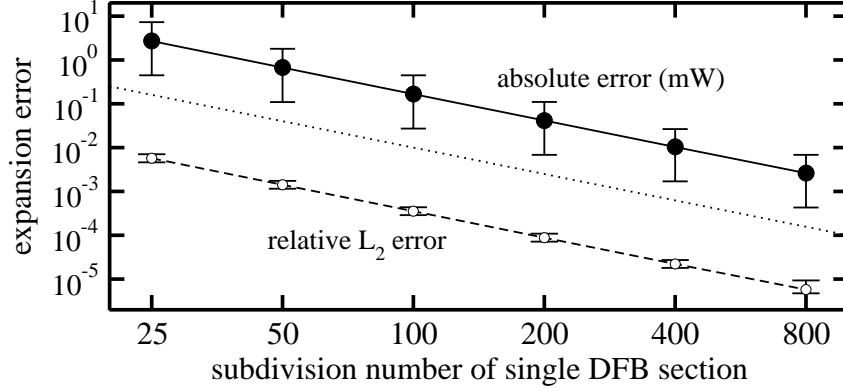

Figure 13: Variation of expansion errors with increasing number of subdivisions. Full bullets: time averaged absolute L_2 space error. Empty bullets: corresponding relative error. Error bars indicate the fluctuations of these errors during the pulsations shown in Fig. 3. The dotted line is given by relation $100(\text{subdivision number})^{-2}$ and indicates a quadratic decay of errors.

To control the precision of our mode expansion (if spontaneous emission $F_{sp}^\pm$ is neglected), to be sure that no one of important modes have been lost and at the same time to check the precision of our numerical integration scheme we compute the absolute and relative L_2 space errors

$$\max_z\left\{\left\|E(z,t) - \sum_{k=1}^q f_k(t)\Theta_E^k(\beta,z)\right\|\right\}, \quad \left\|E(z,t) - \sum_{k=1}^q f_k(t)\Theta_E^k(\beta,z)\right\|\Big/\|E(t)\|.$$

Possible origins of errors are the insufficient finite number of modes used in the field decomposition, errors when estimating integrals of grid functions, and the limited precision of the numerical scheme used for the integration of the TW model. The quadratic relation between errors and discretization step (increased number of section subdivisions) indicates the dominance of integration errors. At the same time this dependence shows an expected correction of computed fields and modes implied by the second order precision numerical scheme. This quadratic decay of errors indicates also the presence of all important modes in the truncated field expansion (8).

Acknowledgments

References

[1] N. Chen, Y. Nakano, K. Okamoto et al:Analysis, Fabrication, and Characterization of Tunable DFB Lasers with Chirped Gratings IEEE Journ. Sel. Topics Quant. Electron. **3**, pp 541 –546 (1997)

[2] M.C. Nowell, L.M. Zhang, J.E. Carroll et al:Chirp reduction using push-pull modulation of three-contact lasers, IEEE Photon. Technol. Lett. **5**, pp 1368 –1371 (1993)

[3] O. Kjebon, R. Schatz, S. Lourdudoss et al:30 GHz direct modulation bandwidth in detuned loaeded InGaAsP DBR-lasers at 1.55 μm wavelength, Electronics Letters **33**, pp 488 –489 (1997)

[4] U. Feiste: Optimization of Modulation Bandwidth in DBR Lasers with Detuned Bragg Reflectors, IEEE J. Quantum Electron. **34**, pp 2371 –2379 (1998)

[5] D.A. Yanson, M.W. Street, S.D. McDougall et al:Terahertz repetition frequencies from harmonic mode-locked monolithic compound-cavity laser diodes Applied Physics Letters **78**, pp 3571 –3573 (2001)

[6] B. Sartorius, C. Bornholdt, O. Brox et al: "All-optical clock recovery module based on a self-pulsating DFB laser", Electron. Lett. **34**, pp 1664 (1998)

[7] M. Radziunas, H.-J. Wünsche, B. Sartorius et al: "Modeling Self-pulsating DFB Lasers with an Integrated Phase Tuning Section", IEEE J. Quantum Electron. **36**, pp 1026 –1034 (2000)

[8] M. Möhrle, B. Sartorius, C. Bornholdt et al:"Detuned Grating Multisection-RW-DFB Lasers for High Speed Optical Signal Processing", IEEE J. Sel. Top. Quantum Electron. **7**, pp 217 –223 (2001)

[9] O. Brox, S. Bauer, M. Radziunas et al:"High-Frequency Pulsations in DFB-Lasers with Amplified Feedback" IEEE J. Quantum Electron. **39(11)**, pp 1381 –1387 (2003)

[10] J.E. Carroll, J.E.A. Whiteaway, R.G.S. Plumb: *Distributed Feedback Semiconductor Lasers*, (IEE Publishing, 1998)

[11] U. Bandelow, M. Radziunas, J. Sieber et al:"Impact of Gain Dispersion on the Spatio-Temporal Dynamics of Multisection Lasers", IEEE J. Quantum Electron. **37**, pp 183 –188 (2001)

[12] M. Radziunas, H.-J. Wünsche, O. Brox et al:"Excitability of a DFB laser with short external cavity", SPIE Proc. Ser. **4646**, pp 420 –428 (2002)

[13] H.-J. Wünsche, O. Brox, M. Radziunas et al:"Excitability of a semiconductor laser by a two-mode homoclinic bifurcation" Phys. Rev. Lett. **88(2)**, pp 23901 (2002)

[14] H.-J. Wünsche, M. Radziunas, S. Bauer, O. Brox, B. Sartorius: "Simulation of Phase-Controlled Mode-Beating Lasers" IEEE J. Sel. Top. Quantum Electron. **9(3)**, pp 857 –864 (2003)

[15] S. Bauer, O. Brox, J. Kreissl et al: "Nonlinear dynamics of semiconductor lasers with active optical feedback", Phys. Rev. E **69**, 016206 (2004)

[16] M. Radziunas, H.-J. Wünsche: "Dynamics of multisection DFB semiconductor laser: traveling wave and mode approximation models", SPIE Proc. Ser. **4646**, pp 27 –37 (2002)

[17] C. Bornholdt, J. Slovak, M. Möhrle et al.: "Application of a 80 GHz all-optical clock in a 160 km transmission experiment", Proceedings OFC **TuN6**, 87 –89 (2002)

[18] G.P. Agrawal, N.K. Dutta: *Long-Wavelength Semiconductor Lasers*, (Van Nostrand Reinhold, New York 1986)

[19] O. Hess, T. Kuhn: Spatio-temporal dynamics of semiconductor lasers: Theory, modelling and analysis. Prog. Quant. Electr. **20(2)**, pp 85 –179 (1996)

[20] D.D. Marcenac: Fundamentals of laser modelling. PhD Thesis, St. Catharine's College, University of Cambridge (1993)

[21] B. Tromborg, H.E. Lassen, H. Olesen: "Travelling Wave Analysis of Semiconductor Lasers," IEEE J. Quantum Electron. **30**, pp 939 –956 (1994)

[22] U. Bandelow, H.-J. Wünsche, B. Sartorius et al: "Dispersive Self-Q-Switching in DFB Lasers – Theory Versus Experiment", IEEE J. Sel. Top. Quantum Electron. **3**, pp 270 –278 (1997)

[23] J. Sieber: Longitudinal Dynamics of Semiconductor Lasers. PhD Thesis, Faculty of Mathematics and Natural Sciences II, Humboldt-University of Berlin (2001)

[24] J. Sieber: "Numerical Bifurcation Analysis for Multi-Section Semiconductor Lasers", SIAM J. on Appl. Dyn. Sys. **1(2)**, pp 248 –270 (2002)

[25] N. Korneyev, M. Radziunas, H.-J. Wünsche et al: "Bifurcations of a DFB Laser with Short Optical Feedback: Numerical Experiment" SPIE Proc. Ser. **4986**, pp 480 –489 (2003)

[26] H. Wenzel, U. Bandelow, H.-J. Wünsche et al: "Mechanisms of fast self pulsations in two-section DFB lasers", IEEE J. Quantum Electron. **32**, pp 69 –79 (1996)

[27] J. Rehberg, H.-J. Wünsche, U. Bandelow et al: "Spectral Properties of a System Describing fast Pulsating DFB Lasers," Z. Angew. Math. Mech. **77(1)**, pp 75 –77 (1997)

[28] M.G. Davis, R.F. O'Dowd: "A transfer matrix method based large signal dynamic model for multielectrode DFB lasers", IEEE J. Quantum Electron. **30**, pp 2458 –2466 (1994)

[29] L.M. Zhang, J.E. Carroll: "Large-signal dynamic model of DFB laser", IEEE J. Quantum Electron. **28**, pp 604 –611 (1992)

[30] B.-S. Kim, Y. Chung, J.-S. Lee: "An efficient split-step time-domain dynamic modeling of DFB/DBR laser diodes", IEEE J. Quantum Electron. **36**, pp 787 –794 (2000)

[31] A.J. Lowery: "New dynamic semiconductor laser model based on the transmission-line modelling method", Proc. Inst. Elect. Eng., pt. J **134(5)**, pp 281 –289 (1987)